International Journal of Hydrogen Energy 149 (2025) 150042

Contents lists available at ScienceDirect

International Journal of Hydrogen Energy

journal homepage: www.elsevier.com/locate/he

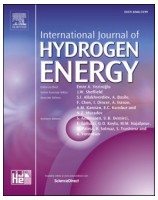

Reactivity of constitution vs. crystallization water under irradiation: Insights from tobermorites

Thibaut Herin [a,b], Antonino Alessi [c,d], Thibault Charpentier [b], Stéphane Poyet [a], Pascal Bouniol [a], Sophie Le Caër [b,*]

[a] Université Paris-Saclay, CEA, Service de Recherche en Corrosion et Comportement des Matériaux, 91191, Gif-sur-Yvette, France
[b] Université Paris-Saclay, CEA, CNRS, NIMBE UMR 3685, 91191, Gif-sur-Yvette, France
[c] LSI, CEA/DRF/IRAMIS, CNRS, Ecole Polytechnique, Institut Polytechnique de Paris, Route de Saclay, F-91128, Palaiseau, France
[d] Department of Physics and Chemistry Emilio Segrè, University of Palermo, Via Archirafi 36, 90123, Palermo, Italy

ARTICLE INFO

Handling Editor: Dr S Nanda

Keywords:
Tobermorite
Cementitious materials
Radiolysis
H_2 production
Paramagnetic defects
Reaction mechanisms

ABSTRACT

Understanding radiolytic H_2 production in irradiated cement is crucial for nuclear waste safety, yet the role of solid cement phases remains unclear. This study examines the behavior of model minerals –tobermorite 11 Å ($Ca_5Si_6O_{17}.5H_2O$) and tobermorite 9 Å ($Ca_5Si_6O_{16}(OH)_2$)- under electron irradiation. When fully dried, these minerals retain only crystallization water or structural hydroxyl groups, respectively. The results reveal that while crystallization water decomposes under irradiation, it does not lead to H_2 formation, as hydrogen atoms react with radiation-induced defects to form SiO–H bonds. In contrast, tobermorite 9 Å produces H_2 only when surface SiO–H bonds are present, indicating that radiolytic dihydrogen arises from surface bond breakage, while the cleavage of the bonds in the material does not ultimately lead to H_2 production. These findings enhance our understanding of irradiation effects on cementitious materials, aiding in the assessment of their long-term stability in nuclear waste storage.

1. Introduction

Although nuclear energy is carbon-free, it generates nuclear waste that needs to be packaged. Cement matrices can be used for this. However, direct exposure of cement to radionuclides may result in the production of radiolytic H_2 and pose a risk to the safety of facilities. Accordingly, a detailed understanding of the reaction pathways leading to dihydrogen production in these materials under irradiation is essential. During the hydration of cement, some of the water added to prepare the cementitious material is consumed to form new hydrated chemical compounds with binding properties. Of these, calcium silicate hydrate (cementitious C–S–H) is the majority phase [1]. The water present in the solid phases is referred to as bound, while the residual liquid water present in the porosity is known as free water. In general terms, radiolytic H_2 is considered to be derived mostly from the decomposition of free water, and the radiolysis of chemically bound water in solid phases is overlooked [2]. However, the fate of the dihydrogen formed, such as its recycling reactions, may be very different depending on whether it is produced in water or in the solid. This distinction is particularly important in the case of cementitious materials, which are heterogeneous composites where pore water interacts intimately with solid hydrates [3]. Moreover, our results highlight the previously underestimated contribution of solid phases to radiolytic dihydrogen production, underscoring the necessity of studying these phases in detail [3]. Thus, the radiolysis of cement hydrates, such as portlandite ($Ca(OH)_2$), has been shown to generate H_2 [4,5]. These findings challenge the conventional assumption that solid components within cement matrices play a negligible role in radiolytic hydrogen production. Table 1 summarizes key literature data on H_2 generation from irradiated cement pastes. The wide variability in the reported apparent radiolytic yields suggests that both the origin of the materials and the thermal treatments applied significantly influence H_2 production, further supporting the need for a systematic investigation into the role of specific solid phases.

The measurements undertaken by Le Caër et al. [7] and Ishikawa et al. [8] on previously-heated pastes (Table 1) show an H_2 production that clearly drops when the relative humidity decreases or the heat treatment temperature is higher. These observations suggest that, in

* Corresponding author.
E-mail address: sophie.le-caer@cea.fr (S. Le Caër).

https://doi.org/10.1016/j.ijhydene.2025.150042
Received 7 March 2025; Received in revised form 11 May 2025; Accepted 14 June 2025
Available online 30 June 2025

Table 1
Radiolytic yields of H_2 production measured in several studies on irradiated cement pastes and calculated relative to the total mass of the samples.

Sample	Treatment prior to irradiation	Ionizing radiation	$G(H_2) \times 10^8$ (mol·J^{-1})	Reference
C–S–H: *Ca/Si* = 1.4	Freeze-dried [b]RH = 30 %	Electrons (10 MeV)	3.3 3.6	[6] [6]
Cement paste (containing cementitious C–S–H and portlandite)	T = 110 °C then[b]RH = 0 %	Electrons (10 MeV)	0.3–0.5	[7]
	T = 110 °C Then[b]RH = 11 %	Electrons (10 MeV)	1.3–2.3	[7]
Cement paste (containing cementitious C–S–H and portlandite)	T = 120 °C T = 40 °C	γ (^{60}Co)	0.06[a] 1.4[a]	[8],[a] [8],[a]
Cement paste (containing cementitious C–S–H and portlandite)		γ (^{60}Co)	3.4	[9]
Cement paste (containing cementitious C–S–H and portlandite)		γ (^{60}Co)	1.0	[10]
C_3S paste (containing cementitious C–S–H and portlandite)	No treatment T = 21 °C	γ (^{60}Co)	2.5[c]	[3]

[a] In the case studied by Ishikawa et al. [8], radiolytic yields were recalculated to take account of the total mass of the samples.
[b] RH = Relative Humidity.
[c] Value after subtracting the contribution of pore water.

previous studies, the majority of the detected H_2 likely originates from the radiolysis of free water -either as pore water or surface-adsorbed water. However, the precise contribution of solid phases remains uncertain, as it is unclear whether free water was fully removed from the cement pastes in those experiments. Similarly, the extent to which the mineral phases within the cement pastes were altered by thermal treatment is unknown. These uncertainties highlight the critical need for well-characterized systems to accurately assess the role of solid phases in radiolytic hydrogen production. It follows that, in a cementitious material, it is important to identify the contribution of cementitious C–S–H to H_2 production under irradiation. Whereas it has been possible to highlight this contribution for portlandite [4,5], it is not currently known for cementitious C–S–H, which nevertheless represents the majority phase of cement and a substantial reservoir of chemically bound water. Unlike portlandite, which contains only water of constitution (O–H bonds), cementitious C–S–H contains water of constitution and water of crystallization (water molecule occupying a defined crystallographic site) [11]. Needless to say, the existence of two types of chemically-bound water (water of constitution and water of crystallization) raises the question of their respective contributions to the production of H_2 under irradiation.

In this context, it is particularly relevant to investigate minerals respectively with one of these two types of water. Moreover, the modeling of cementitious C–S–H, a cryptocrystalline material, by crystallized C–S–H appears natural. Accordingly, tobermorite 9 Å ($Ca_5Si_6O_{16}(OH)_2$), tobermorite 11 Å ($Ca_5Si_6O_{17}.5H_2O$) and tobermorite 14 Å ($Ca_5Si_6O_{16}(OH)_2.7H_2O$) may be thought of as "analogs" of cementitious C–S–H [12–17]. Investigating the radiolysis of these dry crystalline phases requires a controlled desorption step to remove surface-adsorbed water. However, due to the well-documented thermo-hydric instability of tobermorite 14 Å [18–21], we focused our study on the more thermally stable tobermorite 11 Å, which contains only crystallization water. We also included tobermorite 9 Å, obtained by thermally transforming tobermorite 11 Å, as it contains only constitutional water while preserving a closely related crystal structure (see Diagram 1).

The aim of this study is threefold: (i) to synthesize 11 Å and 9 Å tobermorite and prepare them in a desorbed state, free of surface-adsorbed water; (ii) to quantify the radiolytic production of dihydrogen from each phase under ionizing radiation; and (iii) to elucidate the underlying mechanisms by determining how ionizing radiation interacts with crystallization water and constitutional water, respectively.

2. Materials and methods

2.1. Synthesis of materials

Tobermorite 11 Å, with the chemical formula $Ca_5Si_6O_{17}.5H_2O$, was made by adding 4.317 g of tricalcium silicate C_3S (Mineral Research Processing, >99.8 %) [23] and 2.954 g of colloidal silica (Evonik aerosil, >99.8 %, specific surface area 200 m^2 g^{-1}) in a 200 cm^3 hydrothermal reactor. The quantities of materials introduced were chosen so that the molar ratio *Ca/Si* is equal to 5/6. A quantity of pure water (18.2 MΩ cm) was also introduced for obtaining a solid/liquid (mass) ratio equal to 20. The introduction of the reagents and the sealing of the reactor were performed in a glove box purged under a flow of N_2 in order to avoid carbonation phenomena. Once the reactor was sealed, it was heated to 140 °C (p(H_2O) = 36 bar) for a period of 7 days. The resulting powder was then filtered, washed with pure water, and dried under a nitrogen flow for 48 h.

Tobermorite 9 Å (riversideite) with the formula $Ca_5Si_6O_{16}(OH)_2$ was produced by dehydration of tobermorite 11 Å. To do this, tobermorite 11 Å was heated to 290 °C in ambient air for 2 days. This transformation is irreversible. This step removed 4 molecules of water of crystallization and led to a contraction of the interlayer distance, which droped from 11.3 Å to 9.6 Å. The contraction of tobermorite 11 Å (T11) into tobermorite 9 Å (T9) occurs without the formation of secondary phases. The transformation is complete, resulting in the exclusive presence of T9. Heating T9 at 300 °C does not induce structural damage, as this is precisely the temperature required for its formation from T11. This temperature represents the minimum needed for complete contraction; at temperatures above 500 °C, however, T9 undergoes degradation due to the loss of structural water. Notably, the contraction process inherently generates numerous crystallographic defects. Comparison of the X-ray diffraction patterns of T11 and T9 confirms a decrease in crystallinity for T9, as evidenced by fewer and broader diffraction peaks (see Fig. S1 in the Supporting Information).

2.2. Characterization

The products obtained were characterized by means of X-ray diffraction (see Fig. S1 in the SI). ^{29}Si NMR analyses were carried out to obtain information about the atomic connectivity of the materials (see Fig. S2 in the SI).

2.3. Irradiation

Irradiations of tobermorite powders were performed in sealed Pyrex glass ampoules with a volume approximately equal to 10.5 mL. The ampoules were filled with approximately 300 ± 10 mg of powder, which was weighed with precision in advance. The ampoules were then filled with 1.60 bar of ultra-pure argon (99.9999 %). Prior to irradiation, heat treatment was applied directly to the materials in order to desorb the water (see paragraph below). The irradiations were performed with 10 MeV accelerated electrons delivered by the ALIENOR linear accelerator [24]. This accelerator delivers 10 ns pulses providing a dose of approximately 25 Gy (1 Gy = 1 J × kg^{-1}) per pulse with an uncertainty of

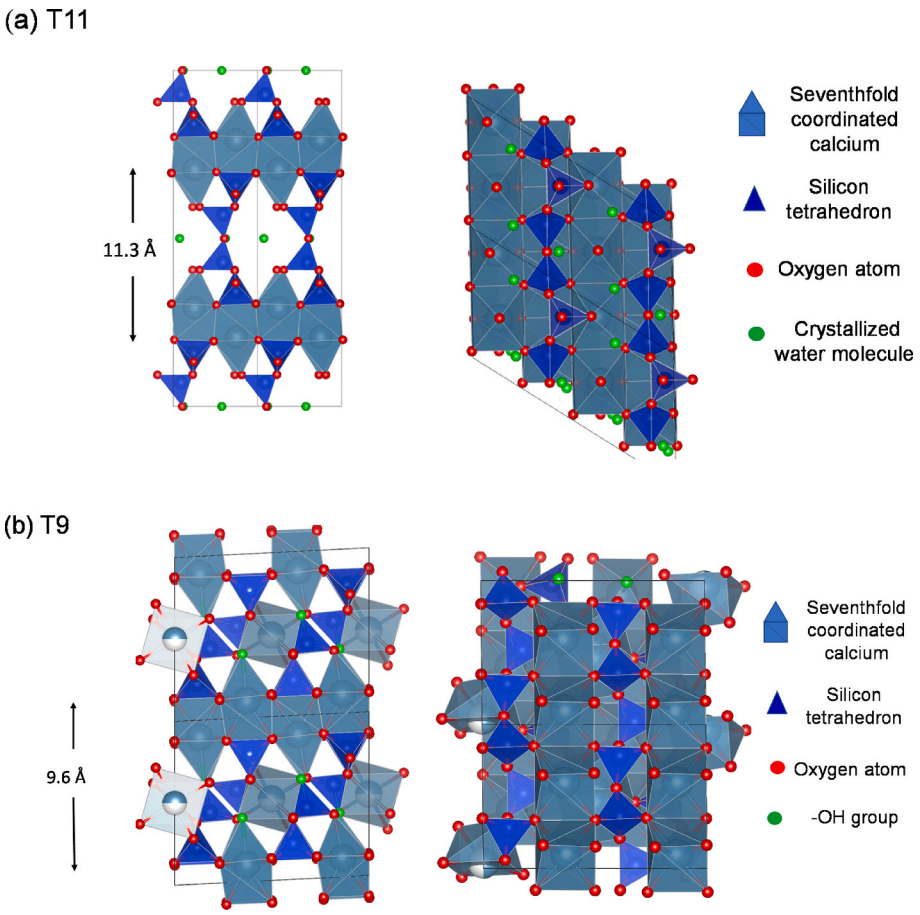

Diagram 1. Diagram of the two tobermorites: (a) T11 and (b) T9. Drawings made using VESTA software [22].

around 5 %. The pulse frequency was restricted to 5 Hz to prevent the samples from heating. Given the stopping power of electrons in crystallized C–S–H and water (ESTAR program [25]), the dose received by the crystallized C–S–H was considered to be, to within 10 %, the same as that received by the water and measured by Fricke dosimetry [26]. More experimental details can be found in Ref. [27].

2.4. Heat treatments

Vacuum heat treatments were carried out directly in the irradiation ampoules to eliminate the adsorbed water so that it was possible to study only the H_2 produced due to the irradiation of the material itself. The aim was also to avoid any contact between the powder and the atmosphere. The ampoules were placed in tubular ovens and connected to a vacuum pump. Two vacuum levels were employed. The primary vacuum (P.V.) is consistent with a vacuum between 0.1 and 1 mbar. The secondary vacuum (S.V.) is consistent with a vacuum of approximately 8 $\times 10^{-4}$ mbar. Unless otherwise stated, the heat treatments were carried out for 16 h. The choice of temperature implies knowledge of the various temperatures at which chemically bound water disappears. Accordingly, thermogravimetric analyses (TGAs) were carried out on the crystallized C–S–H powders.

2.5. TGA analyses

Thermogravimetric analysis (TGA) experiments were performed to control the purity of the tobermorite powders (the presence of carbonate) and to identify their thermal stability range. The experiments were carried out using a Mettler-Toledo TGA/DSC 1 thermogravimeter under nitrogen flow at a flow rate of 50 mL min^{-1}. A 70 μL aluminum oxide crucible was filled with approximately 20 mg of powder. The temperature was raised from 30 °C to 850 °C at a rate of 5 °C.min^{-1}. Given the extremely high quantity of adsorbed water, which may represent from 5 % to 10 % by mass of the materials prior to heat treatment, the mass variations recorded were compared to a theoretical mass (m_{th}), equivalent to the mass of the product without adsorbed water (Eq. (1)). This theoretical mass was calculated using the experimental final mass m_{final} and the theoretical ratio of the molar masses of the final product M_{final} and the initial product $M_{initial}$ (Eq. (2)). Needless to say, this method involves knowing the stoichiometry of the final and initial products.

$$TGA\ (T)result = \frac{m_{experimental}(T)}{m_{th}} \times 100 \quad \text{Eq. 1}$$

$$m_{th} = m_{final} \times \frac{M_{initial}}{M_{final}} \quad \text{Eq. 2}$$

It should be noted that this approach results in an initial mass exceeding 100 % in the presence of adsorbed water or carbonate.

2.6. Measuring H_2 production using gas-phase chromatography (μ-GC)

The H_2 production after irradiation was quantified by micro-gas-phase chromatography (the μGC-R3000 SRA instrument). Ultra-pure argon (99.9999 %) was used as the carrier gas for the analysis. The detection limit of H_2 was10 ppm. Following each analysis, the ampoule atmosphere was renewed and filled with 1.6 bar of ultra-pure argon. This protocol was repeated systematically twice. Several samples were systematically studied to ensure the reproducibility of the results. The uncertainty in the quantities of gas detected was assessed by measuring the standard deviation across the different samples. A minimum intrinsic

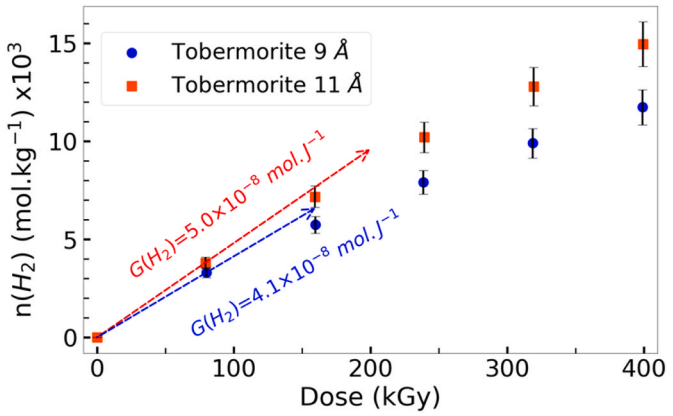

Fig. 1. H_2 production measurements and radiolytic yield of tobermorite 9 and 11 Å in the presence of adsorbed water. Irradiations carried out at room temperature with accelerated electrons of 10 MeV. In tobermorite 11 Å, the H_2 radiolytic yield is equal to $(5.0 \pm 0.4) \times 10^{-8}$ mol.J^{-1}, while it is equal to $(4.1 \pm 0.3) \times 10^{-8}$ mol.J^{-1}in tobermorite 9 Å.

uncertainty of 7 % was also estimated by propagating the different sources of error. When the uncertainty per standard deviation was less than the intrinsic uncertainty, the latter was chosen.

2.7. Electron paramagnetic resonance (EPR) experiments

The EPR spectrometer used was a JEOL JES-X310 with a working frequency of 8.75–9.65 GHz (X band). The modulation frequency was 100 kHz. The spectra were for the most part recorded with a modulation width of 0.05 mT, and for 8 or 15 min. The analysis temperature was varied between −150 °C and 200 °C by means of a thermal regulation device. The powders to be analyzed were introduced into NMR tubes, which were then evacuated and sealed. The irradiation of NMR tubes containing crystallized C–S–H powder resulted in the creation of radiation-induced defects in the glass. However, irradiation with accelerated electrons produced localized irradiation, forming defects at one end of the tube only. The EPR tubes were systematically turned over after irradiation to avoid any superposition of defects present in the glass and those generated in the irradiated crystallized C–S–H powders. This operation meant that the irradiated powder fell into the non-irradiated part of the tube. EPR measurements performed on a test tube without any powder were conducted to confirm the absence of defects detectable by EPR in this part of the tube, and to validate this protocol. The EPR data were analyzed and processed using EasySpin software (Matlab Toolbox) [28,29]. Quantification of the species detected by EPR was carried out in certain situations. This quantification was performed using irradiated alanine powder containing a known number of spins as a control sample. Details of the method have been described in a previous article [5].

2.8. Nuclear magnetic resonance (NMR) measurements

The NMR experiments were performed on a Bruker Avance II NMR spectrometer operating at a magnetic field of 7.05 T (300 MHz, WB magnet). The ^{1}H magic-angle spinning (MAS) NMR data were collected on a 4 mm Bruker CP-MAS probe operating at a spinning frequency of 12.5 kHz. The spectra were measured using the EASY pulse sequence [30] and the spin echo pulse sequence (acquisition 90-τ-180-τ, with τ the echo delay) for suppression of the probe background. The echo delay τ was synchronized with the sample spinning period. The ^{29}Si MAS NMR spectra were acquired using: i) rotor-synchronized spin echo (preceded by a saturation pulse sequence followed by a variable recovery delay); ii) cross-polarization (CPMAS) from ^{1}H nuclei and a typical CP contact time of 2 ms. The data was acquired using Topspin 3.2 software, and

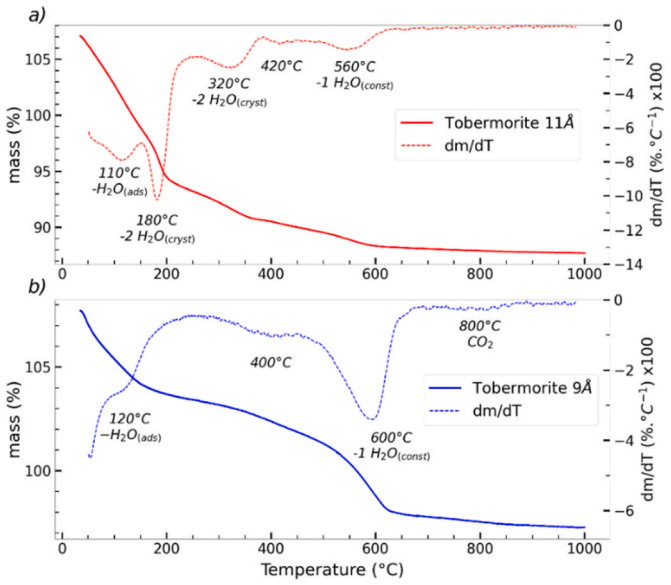

Fig. 2. Thermogravimetric analyses of crystallized tobermorite samples; (a) tobermorite 11 Å; (b) tobermorite 9 Å. Continuous curves: relative mass variation; dotted curves: derivatives of mass variation. Measurements carried out under $N_{2(g)}$ flow at 50 mL min^{-1} with a temperature rise ramp of 5 °C.min^{-1}. H_2O_{const}: breakages of two O–H bonds.

processing was carried out using the latest version of a code developed internally by T. Charpentier [31].

3. Results

3.1. Irradiation in the presence of adsorbed water on the surface of tobermorites

Tobermorite 11 Å and 9 Å powders were first irradiated with accelerated electrons without undergoing any prior desorption treatment. As a result, both samples retained surface-adsorbed water at the time of irradiation. Fig. 1 shows the evolution of cumulative H_2 production for the two tobermorites for a dose ranging from 0 to 400 kGy. The radiolytic yields $G(H_2)$ indicated in Fig. 1 (between 4 and 5 $\times 10^{-8}$ mol.J^{-1}, with the tobermorite 11 Å having a higher yield than the 9 Å) were measured using the slopes of the lines passing through the origin. Indeed, it is clear that production levels are beginning to reach a plateau across this dose range, indicating that the relationship between H_2 production and dose is not linear. Generally, this is due to the fact that H_2 (or its precursors) reacts with radiation-induced defects, leading to so-called H_2 recycling reactions [4]. The radiolytic yield of H_2 production is then defined as the initial slope of the gas evolution curve, representing the amount of hydrogen generated per unit mass of sample as a function of absorbed dose. Accordingly, we determined the yield as the slope at the origin of the curve passing through the first experimental data point; this slope is indicated by a dashed arrow in Fig. 1 (and also in Fig. 4, see below). The values of $G(H_2)$ measured for tobermorite 11 Å and 9 Å are similar to those measured on cement pastes containing free water (Table 1). We should remember, however, that these high values are in large part due to the presence of adsorbed water on the surface of the minerals.

3.2. Desorption treatment

As previously discussed, tobermorites containing surface-adsorbed water exhibit significant radiolytic H_2 production (Fig. 1). To isolate and investigate the specific contribution of chemically bound water -i.e., crystallization or constitutional water- it is therefore essential to

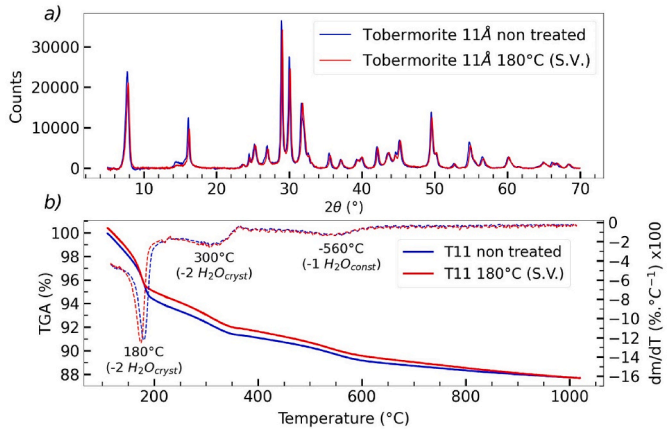

Fig. 3. Comparison of untreated tobermorite 11 Å with tobermorite 11 Å treated for 16 h at 180 °C under secondary vacuum (S.V.). (a) Comparison of the XRD patterns of the untreated tobermorite 11 Å (blue line) and the treated tobermorite 11 Å (red line). (b) Comparison of the TGA profiles and the corresponding derivatives (dotted lines) of the untreated tobermorite 11 Å (blue line) and the treated tobermorite 11 Å (red line). (For interpretation of the references to colour in this figure legend, the reader is referred to the Web version of this article.)

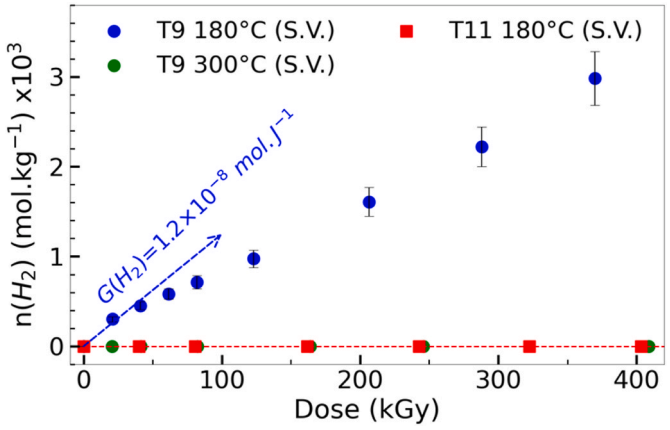

Fig. 4. Measurement of the radiolytic yield of H_2 production of tobermorite 11 Å and tobermorite 9 Å irradiated by accelerated electrons after different heat desorption treatments under secondary vacuum. The radiolytic yield is defined as the slope at the origin of the curve. In tobermorite 9 Å heated at 180 °C under secondary vacuum, the H_2 radiolytic yield is equal to $(1.2 \pm 0.1) \times 10^{-8}$ mol.J^{-1}, while it is below 3×10^{-10} mol.J^{-1} in the other cases.

eliminate any surface-adsorbed water prior to irradiation. Among the methods tested, vacuum heat treatment proved to be the most effective, as alternative approaches did not yield conclusive results. Furthermore, this method has already been successfully employed in the case of portlandite, providing a reliable precedent for its application to C–S–H analogs such as tobermorite [4]. However, a careful balance must be struck when selecting the desorption temperature: it must be high enough to ensure effective removal of surface-adsorbed water, yet low enough to preserve the structural integrity of the minerals. To guide this choice, thermogravimetric analyses (Fig. 2) were performed, providing insight into the thermal stability of the chemically bound water in both tobermorite phases.

The initial masses, significantly greater than 100 % of the theoretical mass (Eq. (2)), and the strong mass variations recorded between 30 °C and 110 °C, reflect the substantial presence of adsorbed water on the surface of the samples. Furthermore, the slight mass variations recorded above 700 °C indicate a very low carbonate content. According to Fig. 2a, tobermorite 11 Å dehydrates in successive steps, which is consistent with the results in the literature [32,33]. Thus, an initial dehydration step, starting at 130 °C and characterized by a significant mass variation peak at 180 °C, is attributed to the loss of two crystallization water molecules. A second, broader peak at 320 °C is associated with the loss of two additional crystallization water molecules. This second step also marks the conversion of tobermorite 11 Å into tobermorite 9 Å. A final mass variation at 560 °C, also visible as a peak at 600 °C on the TGA of tobermorite 9 Å (Fig. 2b), shows the dehydroxylation of SiO–H bonds and the loss of constitution water.

Tobermorite 9 Å is a mineral that is highly resistant to temperature. In fact, dehydroxylation only occurs above 400 °C under TGA conditions (Fig. 2b). Two different desorption treatments were tested to eliminate adsorbed water from the surface of this mineral. In the first, heating was applied at 180 °C under secondary vacuum (S.V.). In the second, the mineral was heated to 300 °C, also under secondary vacuum (S.V.). The samples obtained are called T9-180 and T9-300 respectively. Treatment at 300 °C ensures the dehydroxylation of surface SiO–H bonds. However, a TGA analysis carried out on a sample of T9-300 showed that the mineral still contains a large quantity of SiO–H bonds (see Fig. S3 in Supporting Information).

Tobermorite 11 Å (Fig. 2a) is much more sensitive to temperature than tobermorite 9 Å (Fig. 2b); this is due to the presence of water of crystallization. It follows that it is not possible to heat tobermorite 11 Å above 130 °C without removing some of the crystallization water (Fig. 2a). A heat treatment at 125 °C, performed under primary vacuum for 48 h, was first tested on the tobermorite 11 Å samples. However, the irradiation of these samples leads to H_2 production identical to that of the untreated samples (see Fig. S4 in Supporting Information). This treatment is not enough, therefore, to remove all the adsorbed water on the surface of the tobermorite 11 Å. Nevertheless, the application of a secondary vacuum during the heat treatment unexpectedly increases the thermal stability range. Thus, tobermorite 11 Å samples heated to 180 °C under secondary vacuum exhibit the same XRD pattern as untreated samples (Fig. 3a) and the same TGA profile (Fig. 3b). This shows that these two samples share the same structure and amount of crystallization water, with the adsorbed water removed in the first case. The heightened stability of tobermorite 11 Å when heated in the presence of a high vacuum thus allows efficient desorption of samples without chemically altering the mineral. Subsequently, the tobermorite 11 Å heated to 180 °C under secondary vacuum will be called T11-180. An explanation can be put forward to account for this stability under high vacuum. In fact, the progressive dehydration of tobermorite 11 Å involves a contraction of the interlayer space and its progressive transformation into tobermorite 9 Å. It is possible that the contraction stage is energetically more costly under a high vacuum. This extra energy cost might lead to a higher transition temperature, enabling the crystallization water molecules to withstand higher temperatures than at atmospheric pressure.

3.3. *Measuring H_2 production in dry tobermorite samples*

Both tobermorite 11 Å (T11) and its thermally transformed form, tobermorite 9 Å (T9), possess surface-adsorbed water when exposed to air (Fig. 1). To eliminate the contribution of this surface water to radiolytic H_2 production and isolate the effect of chemically bound water, the samples underwent controlled thermal treatment. Based on thermogravimetric analysis (TGA, Figs. 2 and 3), which provided critical information on the thermal stability of chemically bound water in both tobermorites, appropriate desorption conditions were identified. The powders were placed in hermetically sealed ampoules and heated under secondary vacuum to remove the adsorbed water, then directly irradiated -without any re-exposure to air- to ensure a stable, dry surface state was maintained. For instance, when T9 was treated at 180 °C under vacuum, the resulting sample was designated as T9-180. This notation is used throughout the remainder of the text.

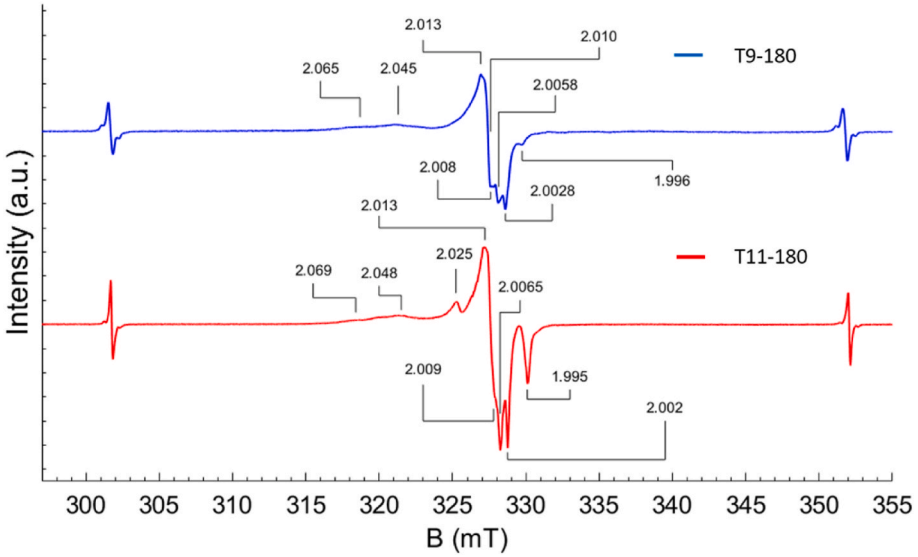

Fig. 5. EPR spectra of a tobermorite 9 Å sample (blue curve, T9-180) and a tobermorite 11 Å sample (red curve) irradiated at 20 kGy in liquid nitrogen by accelerated electrons. Spectra recorded at −150 °C and a power of 1 mW. (For interpretation of the references to colour in this figure legend, the reader is referred to the Web version of this article.)

Fig. 4 shows the radiolytic H_2 production, between 0 and 400 kGy derived from samples of T9-180, T9-300 and T11-180. It is clear that the H_2 production is much lower than the production measured on the untreated minerals (Fig. 1), which confirms that the presence of adsorbed water is largely responsible for the H_2 production observed in Fig. 1. According to Fig. 4, the T11-180 sample does not produce H_2 detectably under irradiation. On the other hand, the T9-180 still shows significant H_2 production. Note that in our case, since T9 is derived from heating T11 (see the Materials and Methods section), the nature and impurity levels are the same in both cases. Therefore, any differences in H_2 production are not attributable to variations in impurity concentrations or nature, but to the change of the material itself. Note, too, that the H_2 production for T9-300 is also undetectable by μ-GC. Undetectable H_2 production corresponds, under our experimental conditions, to a radiolytic yield G(H_2) less than 3×10^{-10} $mol.J^{-1}$.

This absence of H_2 production in T9-300 is interesting in that TGA analyses indicate that this mineral did not undergo significant dehydroxylation of the SiO–H bonds located in the volume of the material. The difference in behavior between the T9-180 and T9-300 could, therefore, be linked to modifications at the surface state of the samples.

3.4. Electron paramagnetic resonance (EPR) analysis

To investigate the radical species formed during irradiation and propose mechanisms responsible for the production or absence of radiolytic H_2, irradiated tobermorite 9 Å and 11 Å samples were analyzed using Electron Paramagnetic Resonance (EPR). Fig. 5 shows the EPR spectra of T9-180 and T11-180 samples irradiated at 20 kGy in liquid nitrogen and then observed by EPR at −150 °C.

The spectra in Fig. 5 are similar. In both cases, it is possible to discern the characteristic doublet of the $H^{\cdot}$ radicals located on either side of a central region (C.R.) with a wealth of paramagnetic defects, and which extends from 310 to 340 mT (Fig. 5). In this region and in both cases, two defects respectively with a component $g_3 \approx 2.065$ and $g_3 \approx 2.045$ for T9-180 and $g_3 \approx 2.069$ and $g_3 \approx 2.048$ for T11-180, are observed. The peaks associated with these two components are broad and very flattened; this suggests that the value of the factor g_3 follows a distribution law. Defects with signals with similar shapes have been observed in silica-based compounds [34–40]. It is reasonable, therefore, to assign the components at $g_3 \approx 2.065$ (T9-180) and $g_3 \approx 2.069$ (T11-180) to $SiO^{\cdot}$ radicals called NBOHCs (non-bridging oxygen hole centers) [34,40]. Other studies, however, suggest that this signal should be attributed to the peroxide ($SiOO^{\cdot}$) radical, abbreviated $SiO_2^{\cdot}$ [34,35]. For the signals at $g_3 = 2.045$ (T9-180) and $g_3 = 2.048$ (T11-180), signals with similar values have been assigned to the peroxide $SiO_2^{\cdot}$ radical [36–39]. The existence of a hole in one of the non-bonding 2p orbitals of an oxygen atom bonding two silicon atoms $Si - O^{\cdot} - Si$ (one type of self-trapped hole, called $STH(1)$) is also a possibility [41]. In general terms, the central regions are very complex, and it was not possible to obtain a precise

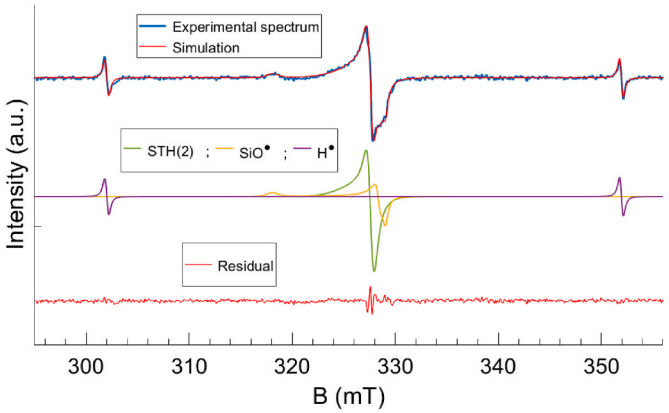

Fig. 6. Decomposition of the experimental annealing spectrum of a T9-180 sample irradiated in liquid nitrogen at 20 kGy and annealed at −130 °C for 80 min. Top lines: experimental spectrum (blue solid line) and modeling (red line); middle lines: decomposition of the spectrum into individual signals. Bottom line: difference between the experimental spectrum and the modeled spectrum. STH(2) is a defect known as a "self-trapped hole" in which the hole is shared by two oxygen atoms. (For interpretation of the references to colour in this figure legend, the reader is referred to the Web version of this article.)

Table 2
Defects making up the simulated EPR spectrum of Fig. 6.

Defect	g_3	g_2	g_1	A (MHz)	Reference
$SiO^{\cdot}$	2.068	2.007	2.002	∅	[34,40]
$STH(2)$	2.024	2.011	2.004	∅	[42]
$H^{\cdot}$		2.003		1391	

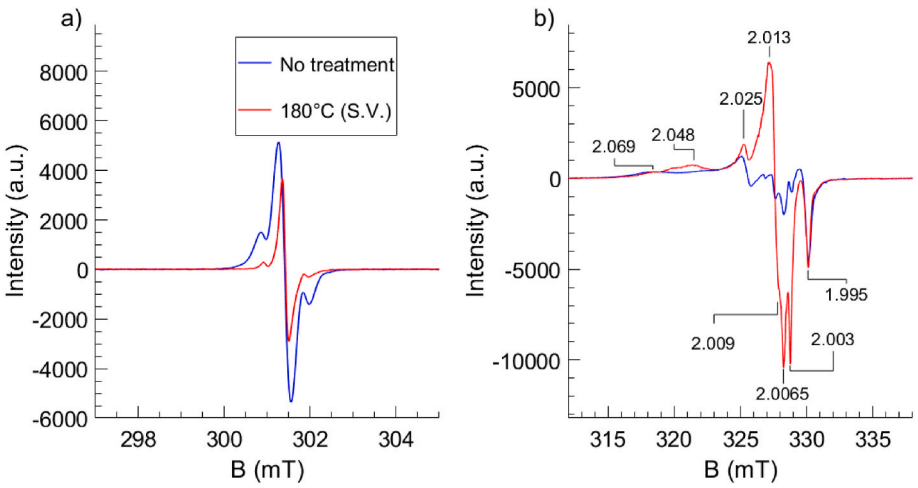

Fig. 7. Influence of desorption treatment on the EPR spectrum of the tobermorite 11 Å sample. Blue curve: untreated tobermorite 11 Å sample; red curve: T11-180. (a) Enlargement of the signal of the $\boldsymbol{H^{\cdot}}$ radicals. For the sake of clarity, only the part of the doublet corresponding to the low field is shown in this figure. (b) Enlargement of the central region. The samples were irradiated in liquid nitrogen at 20 kGy. Spectra recorded at 1 mW and −150 °C on the two samples. (For interpretation of the references to colour in this figure legend, the reader is referred to the Web version of this article.)

decomposition of the different signals that they consist of. Note that there are two types of self-trapped holes. In the first, described above (*STH(1)*), the hole is on an oxygen atom, while for the second (*STH(2)*), the hole is shared by two oxygen atoms [42]. These two defects have close *g* values and are generally both present at low temperatures [42].

One of the key differences between the spectra of the two samples is the presence of an intense negative signal at $g = 1.995$ and a positive signal at $g = 2.025$ on the T11-180 spectrum (Fig. 5). In a study on the radiolysis of cementitious C–S–H, Yin highlighted a defect with a similar shape, and an attribution to a $SiO_2^{\cdot}$ radical was suggested [6]. However, irradiation experiments performed on solid water cooled to −196 °C led to similar signals attributed to hydroxyl $HO^{\cdot}$ radicals [43,44]. In our case, it seems reasonable to attribute these two peaks to $HO^{\cdot}$ radicals present in T11-180 only.

The $H^{\cdot}$ radicals, observed across the spectra of Fig. 5, are not stable and gradually disappear when the temperature increases. This instability is particularly marked in sample T11-180, for which even a temperature of −150 °C is not sufficient to maintain the population of $H^{\cdot}$, which decreases. A 10-min exposure at −100 °C is enough to eliminate all of the $H^{\cdot}$ present in irradiated T11-180. On the other hand, the $H^{\cdot}$ radicals are more stable in T9-180, and a temperature of −150 °C is low enough to stabilize the population of $H^{\cdot}$ radicals. Measurements of the disappearance kinetics of the $H^{\cdot}$ radical were then performed at various temperatures in the T9-180 (Fig. S5 in Supporting Information). These experiments demonstrated that the decay of hydrogen atoms follows a second-order kinetics. The temperature of −130 °C may be thought of as the stability limit of the $H^{\cdot}$ radicals, and the population begins to decay slowly at this temperature (−10 % in 1 h, see Fig. S5 in Supporting Information). The disappearance of the $H^{\cdot}$ radicals in the T9-180 occurs in conjunction with the disappearance of certain defects in the central region. Annealing experiments were performed at −130 °C in order to study the reactivity of $H^{\cdot}$ radicals in this sample. It was then possible to create a virtual spectrum $S_{annealing}(t)$ by subtraction of the first recorded spectrum $S(t=0)$ and a spectrum $S(t)$ recorded at any moment t (Eq. (3)).

$$S_{annealing}(t) = S(t=0) - S(t) \qquad \text{Eq. 3}$$

The $S_{annealing}(t)$ spectrum consists of the signals of the radicals that disappeared during annealing. Fig. 6 shows one $S_{annealing}$ spectrum obtained after an 80 min exposure at −130 °C of a T9-180 sample (blue curve). This $S_{annealing}$ spectrum (80 min) consists of the $H^{\cdot}$ radicals and the defects in the central region that disappeared during the annealing stage. The central region that this spectrum is made up of is simpler and it is possible to model it (red curve). This central region is for the most

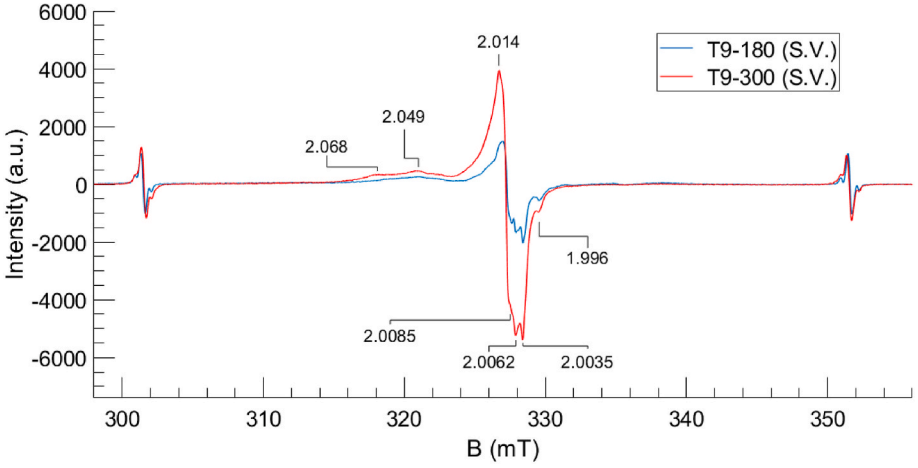

Fig. 8. Comparison of EPR spectra recorded after irradiation at 20 kGy in liquid nitrogen of T9-180 (blue line) and T9-300 (red line). Spectra recorded at −150 °C at a power of 1 mW. (For interpretation of the references to colour in this figure legend, the reader is referred to the Web version of this article.)

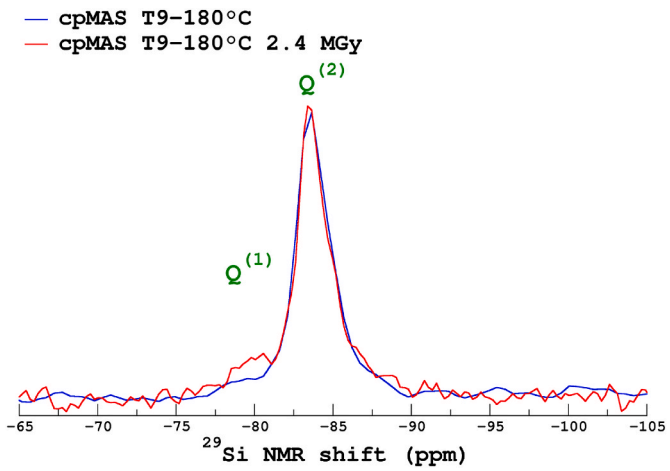

Fig. 9. Comparison of ^{29}Si CPMAS NMR spectra from a sample of non-irradiated T9-180 °C and a sample of T9-180 °C irradiated at 2.4 MGy. Both spectra were normalized to the same maximum height. The Q_1 and Q_2 sites are indicated.

part composed of two signals corresponding to the *SiO*˙ radical and a *STH* (self-trapped hole) radical [42]. A decomposition into individual signals, performed with the EASY-Spin software, is proposed on the graphs located in the center of Fig. 6. The values of the Landé factors, together with their attribution, are summarized in Table 2.

To assess the impact of surface conditions on defect formation, a comparison was made between spectra recorded for desorbed and non-desorbed tobermorite 11 Å samples. This sample was selected due to its high H_2 production in the presence of adsorbed water (Fig. 1) and zero production when desorbed by heating at 180 °C (Fig. 4). Fig. 7 shows the EPR spectra recorded at −150 °C of an untreated tobermorite 11 Å sample (blue curve) containing adsorbed water and that of a T11-180 sample without adsorbed water (red curve). For ease of comparison, Fig. 7a shows an enlargement of the measured part at low field, focusing on the signal of the $H^{\cdot}$ radicals, whereas Fig. 7b focuses on the central region.

Fig. 7a shows that the untreated T11 sample (blue curve) contains more $H^{\cdot}$ radicals than the T11-180 sample. It should equally be noted that it has two small satellite signals on either side of the main signal, signals that are clearly less defined on the T11-180 sample. This suggests the existence of $H^{\cdot}$ radicals present in different chemical environments. It is possible, therefore, that the satellite signals belong to $H^{\cdot}$ derived from the radiolysis of adsorbed water and located on the surface of the material. In contrast, the T11-180 exhibits a spectrum consisting for the most part of a single signal.

The two spectra in Fig. 7b (central region) also have significant differences. The signals are much more intense in the absence of adsorbed water, in line with earlier results that show the effect of the presence of water on the amount of defects produced under irradiation [39,45]. In particular, the defect leading to the intense peak at $g \approx 2.013$ on the T11-180 sample (red curve) appears to be almost absent on the non-desorbed sample (blue curve). This peak at $g \approx 2.013$ is almost certainly a result of the presence of *STH* radicals (Fig. 6). The signal at $g_3 \approx 2.025$ and $g_1 \approx 1.995$, present in both cases, suggests the presence of ***HO***˙ radicals in both samples. The existence of this signal, in similar proportions in the two cases, indicates that it is located in the volume of the material.

According to Fig. 4, the T9-180 and T9-300 exhibit H_2 production that is very different under irradiation. In order to explain this difference, a comparison of the EPR spectra of these two tobermorites is set out in Fig. 8 below.

First, T9-180 and T9-300 have the same quantity of $H^{\cdot}$ radicals. As a result, hydrogen radicals are produced in T9-300, but they do not result in the detectable production of dihydrogen. The defects in the central region are much more intense in T9-300 than in T9-180, as is the case for T11-180 and untreated T11 (Fig. 7). In particular, the peak at $g = 2.014$ is much more intense in T9-300 than in T9-180.

3.5. MAS NMR analysis

To investigate the reaction mechanisms occurring under irradiation, EPR experiments were conducted to identify and characterize the radical species formed. In parallel, ^{29}Si and ^{1}H MAS NMR analyses were performed on samples irradiated at several MGy to gain complementary insight into structural changes. While EPR reveals the nature of the transient paramagnetic species, NMR provides information on the evolution of atomic connectivity (see Figs. 9 and 10, as well as Figs. S6 and S7), shedding light on longer-term structural modifications induced by irradiation. Fig. 9 shows the effect of irradiation at 2.4 MGy on the ^{29}Si CPMAS NMR spectrum of the T9-180. Irradiation at this dose is characterized by a proportion of silicon in Q_1 that is slightly higher than prior to the irradiation (Fig. 9), which implies the breaking of Si–O–Si bonds.

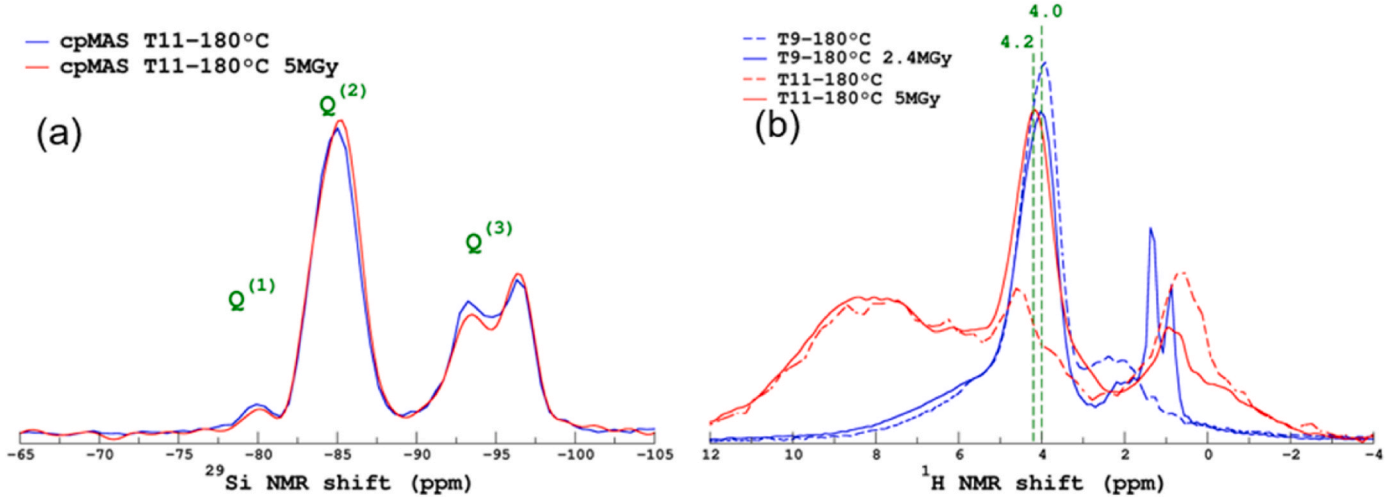

Fig. 10. Effect of 5 MGy irradiation on the NMR spectra of tobermorite 11 Å. Comparison of NMR spectra (a) ^{29}Si and (b) ^{1}H. In Figure (b), the ^{1}H NMR spectra of 9 Å tobermorite before and after irradiation at 2.4 MGy are also provided for comparison. The ^{1}H NMR spectra were recorded with an echo time of 2 ms. Green dashed lines (at 4.0 and 4.2 ppm) serve as a guide for the eyes. Spectra are normalized to the same maximum height. (For interpretation of the references to colour in this figure legend, the reader is referred to the Web version of this article.)

We should remember here that in silicon NMR, the notation Q_n is used to describe the atomic connectivity of SiO_4 tetrahedra in silicate materials. The number n in the notation Q_n represents the number of oxygens shared (or bridging) with other SiO_4 tetrahedra. The presence of Q_1 sites is typical in C–S–H materials and is strongly influenced by the Ca/Si ratio [46]. However, their occurrence in the T9 and T11 samples -characterized by infinite silicate chains- is unexpected. The small amount of Q_1 sites observed in the T9-180 sample may indicate the presence of minor defects (possibly at the surface) or secondary phases, such as poorly ordered C–S–H undetected by XRD, or slight deviations from the ideal Ca/Si stoichiometry [47]. The increase in Q_1 signal following irradiation suggests that bond-breaking processes may have occurred. Nevertheless, due to the complex dynamics of cross-polarization in NMR experiments [48], a precise quantification would require a dedicated MAS NMR study, which is beyond the scope of the present work.

Similar experiments were also performed on T11-180 samples, also showing a small amount of Q_1 species. Fig. 10 shows the effect of irradiation at 5 MGy on the ^{29}Si NMR spectra (Fig. 10a) and ^{1}H spectra (Fig. 10b) of tobermorite 11 Å. According to Fig. 10a, the irradiation only has a slight effect on the ^{29}Si NMR spectrum of tobermorite 11 Å. As a result, irradiation has little influence on the environment and atomic connectivity of silicon atoms. In fact, C–S-Hs are known to be resistant to radiation [49–51]. Indeed, the doses we have used are insufficient to affect the material's structure. This has been particularly demonstrated in cementitious materials by Tajuelo Rodriguez et al. [50] The authors investigated the chemical and structural behavior of synthetic C–S–H following gamma irradiation doses ranging from 0.145 to 0.784 MGy. Comparisons with control samples revealed no significant changes in total water content (measured by thermogravimetric analysis) or basal spacing (determined by X-ray diffraction), indicating that interlayer water remained unaffected by irradiation. Furthermore, irradiation did not alter the material's morphology, C/S ratio, or the mean chain length of the silicate network. In fact, to observe an effect of irradiation on the basal spacing, doses on the order of several tens of MGy are required [51]. Indeed, XRD patterns recorded for T11-180 sample before and after irradiation at 6 MGy show that the diffractograms are highly similar in both cases (Fig. S8 in the Supporting Information).

Fig. 10b presents a comparison of ^{1}H NMR spectra of a non-irradiated and irradiated tobermorite 11 Å and 9 Å. The ^{1}H NMR spectra in Fig. 10b were recorded using a spin-echo acquisition sequence with an echo time of 2 ms (for each sample, spectra acquired at 80 μs, 800 μs and 2 ms are shown in Fig. S6). This allows for a selective attenuation of the signal of the protons contained in the crystallization water molecules, since they have a relaxation time T2 (decaying time of the echo signal) of approximately 100 μs. [52,53]. Fig. 10b shows a signal at 4.2 ppm which is almost absent in the non-irradiated tobermorite 11 Å sample. This signal is very close to a 4.0 ppm signal present in the non-irradiated tobermorite 9 Å sample. According to Fig. S7 (see Supporting Information), the signal recorded at 4.0 ppm in tobermorite 9 Å and at 4.2 ppm in tobermorite 11 Å exhibit identical T2 relaxation times. It follows that these two signals can be assigned to the same type of proton (isolated SiO–H, with no H-bond; see Fig. S7 and the corresponding discussion in the Supporting Information). Moreover, no evidence of H_2 trapping within the structure was found, in contrast to the case of portlandite [4,5].

4. Discussion

One of the most surprising results of this study is the major difference in the H_2 production behavior under ionizing radiation between T11–180, T9-180, and T9-300 (Fig. 4). Unlike the T9-180, the T11-180 does not produce H_2 under irradiation. Moreover, the presence of residual adsorbed water on the T9-180 after treatment at 180 °C under dynamic secondary vacuum for 16 h is to be excluded. In their study on the radiolysis of portlandite, Herin et al. [5] observed that the presence of impurities could significantly affect H_2 production under irradiation. Tobermorite 9 Å, however, is produced by dehydrating tobermorite 11 Å. These two compounds, therefore - with the exception of water - have an identical composition, including even their impurity content. It follows that this hypothesis does not explain the difference in behavior between the two tobermorites. The T9-180 and T11-180 samples intrinsically exhibit different behaviors when subjected to irradiation (Fig. 4), without the desorption protocol or the presence of impurities being responsible for this phenomenon.

EPR analyses (Fig. 5) show that the water of constitution (SiO–H bonds) of tobermorite 9 Å and the water of crystallization of tobermorite 11 Å are decomposed by ionizing radiation. In the case of tobermorite 9 Å and in the absence of adsorbed water, SiO–H bonds represent the sole source of hydrogen atoms. The presence of $H^{\cdot}$ radicals in the EPR spectrum of tobermorite 9 Å (blue curve, Fig. 5) and the highly probable presence of $SiO^{\cdot}$ radicals, characterized by the component $g_3 \approx 2.065$ [34,40], are due to the dissociation of the SiO–H bonds (R. 1):

$$SiO-H \rightarrow SiO^{\cdot} + H^{\cdot} \quad \text{R.1}$$

By the same token, the sole source of hydrogen in T11-180 is derived from hydrogen atoms in crystallization water molecules. The presence of $H^{\cdot}$ and $OH^{\cdot}$ radicals, identified by EPR (red curve, Fig. 5), indicates that a stage of dissociation of the molecules of crystallization water (R. 2) takes place during irradiation. It is important to note that no electron signal was detected by EPR, and reaction R. 2 reflects the species observed experimentally. Indeed, a single water molecule within a well-defined crystallographic site (see Diagram 1a) is not expected to exhibit the same behavior as bulk water.

$$H_2O \rightarrow HO^{\cdot} + H^{\cdot} \quad \text{R.2}$$

In both cases, the irradiation causes the radiolysis of chemically bound water, whether water of constitution or crystallization, which results in the production of $H^{\cdot}$ radicals, precursors of H_2 production. In particular, many studies on the irradiation of solid hydroxides consider the dimerization reaction (R. 3) as a source of H_2 production [54,55]:

$$H^{\cdot} + H^{\cdot} \rightarrow H_2 \quad \text{R.3}$$

H_2 production - or the lack thereof - should be sought in the secondary reactions involving $H^{\cdot}$ radicals, and not in the impossibility of creating these radicals under irradiation. The annealing experiments carried out on T9-180 samples measuring the disappearance kinetics of $H^{\cdot}$ radicals showed that they disappeared based on a second-order kinetics (see Fig. S5 in Supporting Information). Second-order disappearance kinetics assumes that the $H^{\cdot}$ radicals react with a species with an equivalent concentration. Whereas the reaction R. 3 provides evidence of a second-order disappearance kinetics, as well as the H_2 production observed in irradiated T9-180, several experimental facts show that other reactions should be taken into account. In fact, the EPR analyses of the T9-300 indicate that the amount of $H^{\cdot}$ radicals produced under irradiation is similar to that of T9-180 (Fig. 8), while the T9-300 does not produce H_2 (Fig. 4). In addition, the annealing experiments performed on the T9-180 samples (Fig. 6) showed that the disappearance of the $H^{\cdot}$ radicals was accompanied by the simultaneous disappearance of the $SiO^{\cdot}$ and STH(2) radicals. This observation implies that a part of the $H^{\cdot}$ radicals almost certainly disappears by reacting with other defects and, therefore, does not result in H_2 production via R. 3. Quantitative EPR analyses also made it possible to estimate the quantities of radicals disappearing during the annealing process (see Table 3).

According to Table 3, the quantity of $H^{\cdot}$ radicals that disappeared is almost similar to that of the $SiO^{\cdot}$ radicals. This result suggests that the preferred reaction for the disappearance of the $H^{\cdot}$ radicals consists of the reformation of the SiO–H bond via the reaction R. 4.

$$H^{\cdot} + SiO^{\cdot} \rightarrow SiOH \quad \text{R.4}$$

It should be noted that this scenario also implies that the defects

Table 3
Evaluation of the amount of radicals that disappeared during the 80-min annealing at −130 °C of the T9-180 sample irradiated at 20 kGy in liquid dinitrogen.

Defect	$H^{\cdot}$	$SiO^{\cdot}$	$STH(2)$
Quantity lost (***mol***)	8×10^{-10}	9×10^{-10}	1.2×10^{-9}

STH(2) disappear spontaneously without consuming other defects. This is consistent with a well-known problem in SiO_2-based compounds such as quartz or amorphous silica [56]. In fact, the creation of the *STH*(1) and *STH*(2) radicals, produced by an oxygen atom capturing a hole, should be accompanied, by charge conservation, by the production of F centers in similar proportions. In practice, the number of F centers detected is very low compared to the number of trapped holes. This systematic difference has led some authors to hypothesize that many of the electron centers formed in silica are not detectable but may react with the *STH* radicals, resulting in an apparent spontaneous disappearance. It is likely that the reaction R. 4 is predominant compared to the reaction R. 3, and the $H^{\cdot}$ radicals detected by EPR in Fig. 5 do not take part, therefore, in the production of radiolytic H_2. These findings are consistent with the increase in the amount of silicon in Q_1 sites, as shown in the ^{29}Si NMR spectrum in Fig. 9.

It should be noted that the same phenomenon can be observed in tobermorite 11 Å. In fact, EPR analysis (Fig. 5**)** showed the existence of $H^{\cdot}$ radicals. The presence of $HO^{\cdot}$ radicals proves that these radicals are derived from the dissociation of crystallization water molecules via R. 2. Due to their high instability, the disappearance of $H^{\cdot}$ radicals in tobermorite 11 Å could not be investigated as in tobermorite 9 Å. However, this decay occurs without a decrease in the signal belonging to the $HO^{\cdot}$ radicals. This indicates that the radical disappearance pathway $H^{\cdot}$ does not consist of reforming the crystallization water molecules.

This result can be backed up by ^{1}H NMR analyses of the tobermorite 11 Å sample irradiated at 5 MGy (Fig. 10b). In fact, Fig. 10b shows that the ^{1}H NMR spectrum of irradiated tobermorite 11 Å has a signal at 4.1 ppm, which is almost absent in the non-irradiated sample. This signal is very similar to that at 4 ppm measured in the tobermorite 9 Å samples (see Fig. S7 in Supporting Information and the corresponding discussion). It is attributed to the hydrogen atoms of the isolated SiO–H groups, without hydrogen bond interaction with each other [57,58]. Thus, irradiation of tobermorite 11 Å results in the appearance of SiO–H bonds, which is consistent with the results obtained by EPR. Whether in tobermorite 9 Å or tobermorite 11 Å, the $H^{\cdot}$ radicals generated by irradiation recombine with other defects in the structure. In tobermorite 11 Å, this capture of $H^{\cdot}$ radicals prevents the reaction R. 3 and inhibits the production of radiolytic H_2. This capture phenomenon results in the formation of SiO–H bonds, which are initially absent. In tobermorite 9 Å, the SiO–H bonds formed do not necessarily correspond to the original ones, due to the high mobility of the hydrogen atom.

It should be noted that, whereas this explanation helps account for why the T9-300 and the T11-180 do not produce H_2 when subjected to irradiation, it does not explain why T9-180 produces H_2 under ionizing radiation (Fig. 4). A potential explanation is due to a difference in surface state between the two T9 samples. According to a theoretical study by Giraudo et al., [59] a temperature of 270 °C and a pressure of 10^{-3} mbar correspond to the thermodynamic stability limit of the SiO–H bonds of tobermorite 9 Å. These parameters are very similar to the temperature and pressure conditions (300 °C and 8 $\times 10^{-4}$ mbar) used to desorb T9-300 samples. While the conditions set out by Giraudo et al. correspond to thermodynamic stability limits, they do not provide any information about the kinetics of dehydroxylation reactions. Furthermore, the TGA analyses on T9-300 indicate that this mineral still contains a high quantity of SiO–H bonds, almost equivalent to those of the T9-180 (see Fig. S3 in Supporting Information). The only noteworthy difference between the thermogravimetric analyses of the two T9s is related to the slight variation in mass recorded at 380 °C and visible on the T9-180 (Fig. S3 in Supporting Information). In fact, this variation is not present in the T9-300 data. It could be related to the dehydroxylation of surface O–H bonds. This result suggests that, contrary to T9-180, it is likely that the T9-300 no longer contains surface SiO–H bonds. Accordingly, H_2 production in T9-180 could be due exclusively to surface reactions. A first step would be the production of $H^{\cdot}_{surface}$ radicals on the surface of the material:

$$SiOH_{surface} \rightarrow SiO^{\cdot}_{surface} + H^{\cdot}_{surface} \quad \text{R.5}$$

A second step of dimerization of the $H^{\cdot}_{surface}$ radicals would result in the production of H_2:

$$H^{\cdot}_{surface} + H^{\cdot}_{surface} \rightarrow H_{2(g)} \quad \text{R.6}$$

The T9-300 samples exhibit more paramagnetic defects in the central region than the T9-180 samples (Fig. 8**)**. In particular, the defect corresponding to the peak at $g \approx 2.014$ is much less present in the T9-180 samples than in the T9-300 samples (Fig. 8). It should be noted that a similar result was observed on the tobermorite 11 Å (Fig. 7). As a reminder, the EPR signal leading to the intense peak at $g \approx 2.013$ is absent on untreated tobermorite 11 Å samples containing adsorbed water (Fig. 7). It is difficult to explain specifically which defect is responsible for the missing peak at this *g* value. However, the modeling of the annealing spectrum, performed on a T9-180 sample, shows that the radical *STH(2)* (Fig. 5 and Table 2) is a good candidate for explaining this signal. The tobermorite samples with adsorbed water or SiO–H bonds localized on the surface produce fewer defects of type *STH* than the other samples. There are several reasons why this difference may exist. First, it is possible that the *STH* defects are located on the surface. In the presence of adsorbed water, the *STH* defects may react with water molecules. While this hypothesis is enough to explain the difference in the EPR spectra of untreated tobermorite 11 Å and T11-180 (Fig. 7b), it is not sufficient to explain the difference between the T9-180 and the T9-300. In fact, neither the T9-180 nor the T9-300 have adsorbed water on their surface. Accordingly, the absence of *STH* defects in the T9-180 cannot be due to defects located specifically on the surface. An alternative explanation would be to consider that the presence of surface OH bonds on T9-180 (or water adsorbed on tobermorite 11 Å) modifies the reaction mechanisms under irradiation. The irradiation of the materials results first in the formation of holes and electrons in the material (named ionic mechanism in Ref. [60]):

$$irradiation \rightarrow e^- + h^+ \quad \text{R.7}$$

The hole and the electron can be captured by atoms to form secondary species or be correlated by Coulomb interactions to form an exciton:

$$e^- + h^+ \rightarrow exciton \quad \text{R.8}$$

Accordingly, the H_2 production may be the outcome of an ionic (R. 7) or excitonic mechanism (R. 8). The surface state of the material has an influence on the nature of the mechanism involved. The application of a radical heat treatment then results in a change of mechanism, which shifts from excitonic to ionic in silica-based materials [60,61]. This change in mechanism is linked to the dehydroxylation of the materials, and a drop in the H_2 production under irradiation is then observed [60, 61]. It is possible that the existence of SiO–H bonds or water molecules on the surface of the material allows a transfer of the energy deposited in the matter by excitonic means (R. 9).

$$SiOH + exciton \rightarrow SiO^{\cdot} + H^{\cdot} \quad \text{R.9}$$

Following a more drastic heat treatment, the ionic mechanism is favored. The presence of this mechanism results in the formation of h^+ holes that can be captured by Si–*O*–Si bonds to form a *STH* radical. In the case of the tobermorites, the presence of adsorbed water or surface SiO–H bonds would enable an excitonic mechanism, resulting in significant H_2 production and a decrease in the number of *STH(2)*-type

defects. It should be noted that the existence of an excitonic mechanism allows the efficient transfer of the energy deposited in the volume to the surface (R. 9). It is likely that this property explains why the radiolytic yields measured in the presence of adsorbed water are so high (Fig. 1). In the absence of surface bonds, this mechanism is replaced by an ionic mechanism, which leads to the formation of a large number of *STH* radicals in the irradiated T9-300.

5. Conclusion

Two well-crystallized tobermorites −9 Å and 11 Å- were investigated to gain new insight into the radiolysis of chemically bound water in cementitious calcium silicate hydrate (C–S–H) phases. These minerals were selected because they contain distinct forms of bound water: tobermorite 9 Å incorporates constitution water, while tobermorite 11 Å contains only crystallization water. Uniquely, both samples share the same chemical composition (Ca/Si ratio, impurity levels) and similar structural frameworks, providing a rare opportunity to isolate and compare the behavior of these two types of bound water under controlled irradiation conditions.

The use of "high-temperature" vacuum treatments enabled obtaining samples completely free of adsorbed water, thereby allowing for a clear distinction between the contributions of structural water alone. Remarkably, irradiation experiments revealed that crystallization water in tobermorite 11 Å does not lead to dihydrogen (H_2) production. In contrast, tobermorite 9 Å, which is derived from heat-treated tobermorite 11 Å and retains SiO–H surface groups, does produce H_2 -provided the thermal treatment is mild enough to preserve these surface hydroxyls. This unexpected outcome highlights the critical role of surface chemistry in radiolytic hydrogen production.

EPR measurements confirmed that radiolysis of both constitution and crystallization water occurs, generating $H^\bullet$ radicals in the mineral matrix. However, H_2 formation is not guaranteed. Instead, $H^\bullet$ radicals can be trapped by structural defects, forming stable species such as SiO–H groups in the bulk. This finding leads to the conclusion that radiolytic H_2 production in these systems is primarily a surface-driven process, with little or no contribution from the mineral volume. Consequently: (i) significant H_2 yields are observed only in the presence of adsorbed water, and (ii) only tobermorite 9 Å, which retains reactive SiO–H groups on the surface, produces H_2 under irradiation. Analogous to observations in irradiated silica and quartz, this surface-specific H_2 production may result from excitonic mechanisms enabling energy transfer from the bulk to the surface. When thermal treatment is too aggressive, the mechanism shifts from excitonic to ionic, introducing a high density of defects but suppressing H_2 generation.

In conclusion, the radiolysis of the crystallization water of the tobermorites does not result in the production of radiolytic H_2. Only surface SiO–H bonds produce H_2 under irradiation. Based on the assumption that the behavior of the cementitious, cryptocrystalline C–S–H follows the same principles demonstrated in the two types of tobermorite studied, the radiolytic H_2 production of this material should be relatively limited. It would be even weaker since the cementitious C–S–H is not in powder form (which, in fact, exacerbates the surface phenomena), but in massive form. The H_2 source term associated with cementitious C–S–H could thus not exceed that of the portlandite or could even be significantly lower. Following the results obtained for the portlandite, these results pave the way to considering solid phases in a more comprehensive modeling of the radiolysis of cementitious materials.

CRediT authorship contribution statement

Thibaut Herin: Writing – original draft, Methodology, Investigation, Formal analysis, Data curation, Conceptualization. **Antonino Alessi:** Writing – review & editing, Writing – original draft, Validation, Supervision, Methodology, Investigation, Conceptualization. **Thibault Charpentier:** Writing – review & editing, Validation, Supervision, Methodology, Investigation, Formal analysis, Conceptualization. **Stéphane Poyet:** Writing – review & editing, Writing – original draft, Validation, Supervision, Project administration, Methodology, Funding acquisition, Formal analysis, Data curation, Conceptualization. **Pascal Bouniol:** Writing – review & editing, Writing – original draft, Validation, Supervision, Project administration, Methodology, Investigation, Funding acquisition, Formal analysis, Conceptualization. **Sophie Le Caër:** Writing – review & editing, Writing – original draft, Validation, Supervision, Project administration, Methodology, Investigation, Funding acquisition, Data curation, Conceptualization.

Declaration of competing interest

The authors declare the following financial interests/personal relationships which may be considered as potential competing interests: HERIN Thibaut reports financial support was provided by French Alternative Energies and Atomic Energy Commission Administrative Headquarters. LE CAER Sophie reports financial support was provided by EDF (France). POYET Stephane reports financial support was provided by EDF (France). If there are other authors, they declare that they have no known competing financial interests or personal relationships that could have appeared to influence the work reported in this paper.

Acknowledgements

We would like to express our gratitude to EDF and CEA for their financial support. We would like to thank Jorge Vieira for his help during the irradiation experiments with the ALIENOR linear accelerator. In addition, we would like to thank the EMIR&A network, as well as Audrey Courpron and Ozlem Oral for the EPR experiments.

Appendix A. Supplementary data

Supplementary data to this article can be found online at https://doi.org/10.1016/j.ijhydene.2025.150042.

References

[1] Lothenbach B, Matschei T, Möschner G, Glasser FP. Thermodynamic modelling of the effect of temperature on the hydration and porosity of portland cement. Cement Concr Res 2008;38:1–18.
[2] Bouniol P, Bjergbakke E. A comprehensive model to describe radiolytic processes in cement medium. J Nucl Mater 2008;372:1–15.
[3] Bouniol P. Contribution of the tricalcium silicate hydration products to the formation of radiolytic H_2: a systemic approach. J Adv Concr Technol 2022;20:72–84.
[4] Herin T, Charpentier T, Bouniol P, Le Caër S. Behavior of portlandite upon exposure to ionizing radiation: evidence of delayed H_2 production. J Phys Chem C 2023;127:20245–54.
[5] Herin T, Alessi A, Poyet S, Bouniol P, Le Caër S. H_2 production mechanisms in irradiated portlandite: surface and volume contributions. J Phys Chem C 2024;128:19529–40.
[6] Yin C. Hydrogen production from irradiated calcium silicate hydrate. Université Paris Saclay; 2019.
[7] Le Caër S, et al. Production of H_2 by water radiolysis in cement paste under electron irradiation: a joint experimental and theoretical study. Cement Concr Res 2017;100:110–8.
[8] Ishikawa S, Maruyama I, Takizawa M, Etoh J, Kontani O, Sawada S. Hydrogen production and the stability of hardened cement paste under gamma irradiation. J Adv Concr Technol 2019;17:673–85.
[9] Möckel HJ, Köster RH. Gas Formation during the gamma radiolysis of cemented low- and intermediate-level waste products. Nucl Technol 1982;59:494–7.
[10] Chartier D, Sanchez-Canet J, Bessette L, Esnouf S, Renault JP. Influence of formulation parameters of cement based materials towards gas production under gamma irradiation. J Nucl Mater 2018;511:183–90.
[11] Roosz C, Gaboreau S, Grangeon S, Prêt D, Montouillout V, Maubec N, Ory S, Blanc P, Vieillard P, Henocq P. Distribution of water in synthetic calcium silicate hydrates. Langmuir 2016;32:6794–805.
[12] Richardson IG, Groves GW. Models for the composition and structure of calcium silicate hydrate (C-S-H) gel in hardened tricalcium silicate pastes. Cement Concr Res 1992;22:1001–10.
[13] Cong X, Kirkpatrick RJ. ^{29}Si MAS NMR study of the structure of calcium silicate hydrate. Adv Cement Base Mater 1996;3:144–56.

[14] Richardson IG. Tobermorite/jennite- and tobermorite/calcium hydroxide-based models for the structure of C-S-H: applicability to hardened pastes of tricalcium silicate, B-dicalcium silicate, portland cement, and blends of portland cement with blast-furnace slag, metakaolin, or silica fume. Cement Concr Res 2004;34:1733–77.
[15] Pellenq RJ-M, Kushima A, Shahsavari R, Van Vliet KJ, Buehler MJ, Yip S, Ulm F-J. A realistic molecular model of cement hydrates. Proc Natl Acad Sci USA 2009;106:16102–7.
[16] Grangeon S, Claret F, Roosz C, Sato T, Gaboreau S, Linard Y. Structure of nanocrystalline calcium silicate hydrates: insights from X-ray diffraction, synchrotron X-ray absorption and nuclear magnetic resonance. J Appl Crystallogr 2016;49:771–83.
[17] Grangeon S, Fernandez-Martinez A, Baronnet A, Marty N, Poulain A, Elkaïm E, Roosz C, Gaboreau S, Henocq P, Claret F. Quantitative X-ray pair distribution function analysis of nanocrystalline calcium silicate hydrates: a contribution to the understanding of cement chemistry. J Appl Crystallogr 2017;50:14–21.
[18] Farmer VC, Jeevaratnam J, Speakman K, Taylor HFW. Thermal decomposition of 14 Å tobermorite from crestmore. REt EIVED 1966;291.
[19] Gmira A, Pellenq RJM, Rannou I, Duclaux L, Clinard C, Cacciaguerra T, Lequeux N, Van Damme H. A structural study of dehydration/rehydration of tobermorite, a model cement compound. In: Rodriguez-Reinoso F, McEnaney B, Rouquerol J, Unger K, editors. Stud. Surf. Sci, vol. 144. Elsevier; 2002. p. 601–8. Catal.
[20] Bonaccorsi E, Merlino S, Kampf AR. The crystal structure of tobermorite 14 Å (plombierite), a C–S–H phase. J Am Ceram Soc 2005;88:505–12.
[21] Biagioni C, Bonaccorsi E, Merlino S, Bersani D. New data on the thermal behavior of 14 Å tobermorite. Cement Concr Res 2013;49:48–54.
[22] Momma K, Izumi F. Vesta 3 for three-dimensional visualization of crystal, volumetric and morphology data. J Appl Crystallogr 2011;44:1272–6.
[23] Li X, Hu Q, Robertson B, Ley MT, De Andrade VJ, Sokhansefat G. Direct observation of C_3S particle dissolution using fast nano X-ray computed tomography. Cement Concr Res 2023;166:107097.
[24] Mialocq JC, Hickel B, Baldacchino G, Juillard M. The radiolysis Project of cea. J. Chim. Phys. 1999;96:35–43.
[25] Berger MJ, Coursey JS, Zucker MA, Chang J. Estar, pstar, and astar: computer programs for calculating stopping-power and range tables for electrons. *Protons, and helium ions*, 1.2.3. Gaithersburg, MD: National Institute of Standards and Technology; 2005. https://physics.nist.gov/Star.
[26] Fricke H, Hart EJ. Chemical dosimetry. In: Attix FH, Roesch WC, editors. Radiation dosimetry. second ed.vol. 2. New York and London: Academic press; 1966. p. 167–232.
[27] Cataldo T, Charpentier T, Landrot G, Chua S, Bedford NM, Veliscek-Carolan J, Le Caër S. Probing the high radiation tolerance of minor actinide selective zirconium phosphonate sorbents. J Mater Chem A 2025;13:8666–78.
[28] Stoll S, Schweiger A Easyspin. A comprehensive software package for spectral simulation and analysis in epr. J Magn Reson 2006;178:42–55.
[29] Stoll S. Chapter six - CW-EPR spectral simulations: solid state. In: Qin PZ, Warncke K, editors. Methods in enzymology, vol. 563. Academic Press; 2015. p. 121–42.
[30] Jaeger C, Hemmann F Easy. A simple tool for simultaneously removing background, deadtime and acoustic ringing in quantitative NMR spectroscopy–Part I: basic principle and applications. Solid State Nucl Magn Reson 2014;57–58:22–8.
[31] Charpentier, T., PhD thesis, Orsay, France, 1998.
[32] Yu P, Kirkpatrick RJ. Thermal dehydration of tobermorite and jennite. Concr. Sci. Engin. 1999;1:185–91.
[33] Pourbeik P, Beaudoin JJ, Alizadeh R, Raki L. Drying of calcium-silicate-hydrates: regeneration of elastic modulus. Adv Cement Res 2015;27:470–6.
[34] Stapelbroek M, Griscom DL, Friebele EJ, Sigel Jr, GH. Oxygen-associated trapped-hole centers in high-purity fused silicas. J Non-Cryst Solids 1979;32:313–26.
[35] Friebele EJ, Griscom DL, Stapelbroek M, Weeks RA. Fundamental defect centers in glass: the peroxy radical in irradiated, high-purity, fused silica. Phys Rev Lett 1979;42:1346–9.
[36] Dutt DA, Higby PL, Griscom DL. An electron spin resonance study of X-irradiated calcium aluminosilicate glasses. J Non-Cryst Solids 1991;130:41–51.
[37] Boizot B, Petite G, Ghaleb D, Calas G Dose. Dose rate and irradiation temperature effects in B-irradiated simplified nuclear waste glasses by EPR spectroscopy. J Non-Cryst Solids 2001;283:179–85.
[38] Chah K, Boizot B, Reynard B, Ghaleb D, Petite G. Micro-Raman and EPR studies of B-radiation damages in aluminosilicate glass. Nucl Instrum Methods Phys Res B 2002;191:337–41.
[39] Le Caër S, Rotureau P, Brunet F, Charpentier T, Blain G, Renault JP, Mialocq J-C. Radiolysis of confined water: hydrogen production at a high dose rate. ChemPhysChem 2005;6:2585–96.
[40] Skuja L, Kajihara K, Hirano M, Hosono H. Oxygen-excess-related point defects in glassy/amorphous SiO_2 and related materials. Nucl Instrum Methods Phys Res B 2012;286:159–68.
[41] Griscom DL. Self-trapped holes in amorphous silicon dioxide. Phys Rev B 1989;40:4224–7.
[42] Griscom DL. Self-trapped holes in pure silica glass: a history of their discovery and characterization and an example of their critical significance to industry. J Non-Cryst Solids 2006;352.
[43] Johnson JE, Moulton GC. Esr study of ice irradiated at 4.2 K, a thermally reversible radical. J Chem Phys 1978;69:3108–11.
[44] Riederer H, Hüttermann J, Boon P, Symons MCR. Hydroxyl radicals in aqueous glasses: characterization and reactivity studied by ESR spectroscopy. J Magn Reson 1983;54:54–66.
[45] Lainé M, Balan E, Allard T, Paineau E, Jeunesse P, Mostafavi M, Robert J-L, Le Caër S. Reaction mechanisms in swelling clays under ionizing radiation: influence of the water amount and of the nature of the clay mineral. RSC Adv 2017;7:526–34.
[46] Brunet F, Bertani P, Charpentier T, Nonat A, Virlet J. Application of ^{29}Si homonuclear and ^{1}H-^{29}Si heteronuclear NMR correlation to structural studies of calcium silicate hydrates. J Phys Chem B 2004;108:15494–502.
[47] Wieker W, Grimmer AR, Winkler A, Mägi M, Tarmak M, Lippmaa E. Solid-state high-resolution ^{29}Si NMR spectroscopy of synthetic 14 Å, 11 Å and 9 Å tobermorites. Cement Concr Res 1982;12:333–9.
[48] Klur I, Jacquinot J-F, Brunet F, Charpentier T, Virlet J, Schneider C, Tekely P. NMR cross-polarization when tis > T1r; examples from silica gel and calcium silicate hydrates. J Phys Chem B 2000;104:10162–7.
[49] Mobasher N, Bernal SA, Kinoshita H, Sharrad CA, Provis JL. Gamma irradiation resistance of an early age slag-blended cement matrix for nuclear waste encapsulation. J. Mat. Res. 2015;30:1563–71.
[50] Tajuelo Rodriguez E, Hunnicutt WA, Mondal P, Le Pape Y. Examination of gamma-irradiated calcium silicate hydrates. Part I: chemical-structural properties. J Am Ceram Soc 2020;103:558–68.
[51] Baral A, Tajuelo Rodriguez E, Hunnicutt WA, Cakmak E, Sun H, Ilavsky J, Le Pape Y, Rosseel TM, Garg N. Ultra-high gamma irradiation of calcium silicate hydrates: impact on mechanical properties, nanostructure, and atomic environments. Cement Concr Res 2022;158:106855.
[52] Holly R, Reardon EJ, Hansson CM, Peemoeller H. Proton spin–spin relaxation study of the effect of temperature on white cement hydration. J Am Ceram Soc 2007;90:570–7.
[53] Muller ACA, Scrivener KL, Gajewicz AM, McDonald PJ. Densification of C–S–H measured by ^{1}H NMR relaxometry. J Phys Chem C 2013;117:403–12.
[54] Lainé M, Balan EA, Th, Martin F, von Bardeleben H-J, Robert J-L, Le Caër S. Reaction mechanisms in talc under ionizing radiation: evidence of a high stability of $H^{\bullet}$ atoms. J Phys Chem C 2016;120:2087–95.
[55] Kaddissy JA, Esnouf S, Durand D, Saffre D, Foy E, Renault J-P. Radiolytic events in nanostructured aluminum hydroxides. J Phys Chem C 2017;121:6365–73.
[56] Griscom DL. Trapped-electron centers in pure and doped glassy silica: a review and synthesis. J Non-Cryst Solids 2011;357:1945–62.
[57] Rawal A, Smith BJ, Athens GL, Edwards CL, Roberts L, Gupta V, Chmelka BF. Molecular silicate and aluminate species in anhydrous and hydrated cements. J Am Chem Soc 2010;132:7321–37.
[58] Hayashi S, Kojima N. Acid properties of H-type mordenite studied by solid-state NMR. Microporous Mesoporous Mater 2011;141:49–55.
[59] Giraudo N, Bergdolt S, Laye F, Krolla P, Lahann J, Thissen P. Dehydration and dehydroxylation of C-S-H phases synthesized on silicon wafers. Appl Surf Sci 2018;433:589–95.
[60] Thomas JK. Physical aspects of radiation-induced processes on SiO_2, gamma-Al_2O_3, zeolites and clays. Chem Rev 2005;105:1683–734.
[61] Zhang G, Mao Y, Thomas JK. Surface chemistry induced by high energy radiation in silica of small particle structures. J Phys Chem B 1997;101:7100–13.